

Chiral europium halides with high-performance magnetic field tunable red circularly polarized luminescence at room temperature

Received: 5 January 2025

Accepted: 20 February 2025

Published online: 14 March 2025

 Check for updates

Xinyi Niu^{1,7}, Yang Li^{2,3,7}, Haolin Lu¹, Zhaoyu Wang¹, Yunxin Zhang¹, Tianyin Shao¹, Hebin Wang¹, Sehrish Gull¹, Bing Sun⁴, Hao-Li Zhang⁴, Yongsheng Chen^{5,6}, Kai Wang^{2,3}✉, Yaping Du¹✉ & Guankui Long¹✉

Chiral organic-inorganic hybrid metal halides as promising circularly polarized luminescence (CPL) emitter candidates hold great potential for high-definition displays and future spin-optoelectronics. The recent challenge lies primarily in developing high-performance red CPL emitters. Here, coupling the $f-f$ transition characteristics of trivalent europium ions (Eu^{3+}) with chirality, we construct the chiral Eu-based halides, $(R/S\text{-}3\text{BrMBA})_3\text{EuCl}_6$, which exhibit strong and predictable red emission with large photoluminescence quantum yield (59.8%), narrow bandwidth (≈ 2 nm), long lifetime (≈ 2 ms), together with large dissymmetry factor $|g_{\text{lum}}|$ of 1.84×10^{-2} . Compared with the previously reported chiral metal halides, these chiral Eu-based halides show the highest red CPL brightness. Furthermore, the degree of photoluminescence polarization in $(R/S\text{-}3\text{BrMBA})_3\text{EuCl}_6$ can be manipulated by the external magnetic field. Particularly, benefiting from the field-generated Zeeman splitting and spin mixing at exciton states, an anomalously positive magneto-photoluminescence was observed at room temperature. This work provides an efficient strategy for constructing both high-performance and pure-red CPL emitters. It also opens the door for chiral rare-earth halides toward chiral optoelectronic and spintronic applications.

Circularly polarized luminescence (CPL) emitters are prospective for diverse applications, including three-dimensional (3D) displays¹, optical anti-counterfeiting², information encryption^{3,4}, biological probes⁵, and circularly polarized light-emitting diodes (CP-LEDs)^{6–12}. Recently, chiral organic-inorganic hybrid metal halides have emerged as promising CPL emitters due to their excellent chiroptical effects, high photoluminescence quantum yield (PLQY), and versatile solution processing strategies^{13–34}. Red light, as one of the three primary colors of light, can regulate all visible light signals together with green and blue light, which is crucial for CPL emitters in high-definition 3D

displays^{35–38}. However, it remains a great challenge to construct the chiral hybrid metal halides to obtain both efficient and pure-red CPL. Existing studies on red-CPL emitters mostly focus on the chiral manganese-based hybrid metal halides^{39–43}. Despite the remarkable performance achieved by these materials, they still suffer from broad emission peaks which result in insufficient color purity⁴⁴. Moreover, accurately predicting the emission bands for traditional chiral hybrid metal halides is still extremely challenging, as the complicated coordination environment deeply influences the luminescent color. Thus, developing novel strategies to construct the chiral hybrid metal

A full list of affiliations appears at the end of the paper. ✉ e-mail: kaiwang@bjtu.edu.cn; ypdu@nankai.edu.cn; longgk09@nankai.edu.cn

halides with both high color purity and predictable red emission is highly needed.

Rare-earth ions with $4f-4f$ transitions, as ideal luminescent centers, have garnered significant interest owing to their exceptional features, such as high color purity, large Stokes shift, and long excited state lifetime of millisecond level^{45–48}. More importantly, the $4f$ orbitals of rare-earth ions are shielded by the outside $5s^2$ and $5p^6$ electrons⁴⁶, weakening the influence of the surrounding environment on the $4f$ orbitals, resulting in the sharp and narrow line-like fingerprint emission^{44,49}. As a result, these rare-earth materials possess predictable luminescent wavelengths together with high color purity. Among the rare-earth ions, the trivalent europium ion (Eu^{3+}) with both large PLQY and high color purity in the red emission region has attracted the attention of broader research community in various fields, such as color television screens⁵⁰, anti-counterfeiting inks², and luminescent probes towards biochemical applications⁵¹. Therefore, it is highly desirable to construct the Eu-based chiral hybrid metal halide to achieve both the efficient and pure-red CPL.

In this work, we have designed and constructed the chiral Eu-based hybrid metal halides, namely, $(R/S-3\text{BrMBA})_3\text{EuCl}_6$ (3BrMBA = 1-(3-bromophenyl)ethylammonium), through an anti-solvent assisted crystallization method. By coupling the $4f-4f$ transition properties of Eu^{3+} ions with chirality, these chiral Eu-based halides exhibit both efficient and narrow-band red photoluminescence (≈ 2 nm), high color purity and PLQY (59.8%), together with large dissymmetry factor $|g_{\text{lum}}|$ of 1.84×10^{-2} . Compared with the previously reported chiral metal halides with red CPL emission, these chiral Eu-based halides exhibit the highest CPL brightness. In addition, the degree of photoluminescence polarization (DP) of $(R/S-3\text{BrMBA})_3\text{EuCl}_6$ can be effectively manipulated and enhanced by the external magnetic field. An unusual positive magneto-photoluminescence (MPL) at room temperature was also

observed in these chiral Eu-based hybrid metal halides, which is attributed to the field-generated Zeeman splitting and spin mixing at exciton states. This work provides a feasible strategy for developing both the efficient and pure-red CPL emitter based on chiral rare-earth halides and lays the foundation for their applications in chiral optoelectronics and spintronics.

Results

Material properties

The crystal structures of the as-synthesized $(R-3\text{BrMBA})_3\text{EuCl}_6$ and $(S-3\text{BrMBA})_3\text{EuCl}_6$ were determined by the single-crystal X-ray diffraction (SCXRD), and both of them crystallized in the orthorhombic *Sohncke* space group of $P2_12_12_1$. As shown in Fig. 1a, they are typical zero-dimensional (0D) structures with each $[\text{EuCl}_6]^{3-}$ octahedron surrounded by three chiral $R/S-3\text{BrMBA}^+$ cations. Owing to the enantiomeric nature, the lattice constants of $(R-3\text{BrMBA})_3\text{EuCl}_6$ and $(S-3\text{BrMBA})_3\text{EuCl}_6$ are almost the same (Supplementary Table 1). Most importantly, the space group of the inorganic frameworks for $(R/S-3\text{BrMBA})_3\text{EuCl}_6$ after removing the chiral $R/S-3\text{BrMBA}^+$ cations is still $P2_12_12_1$ (Supplementary Fig. 1), which suggests that the chirality is transferred to the inorganic frameworks by chiral induction⁵². The powder X-ray diffraction (PXRD) patterns are consistent with the simulated results, demonstrating the high phase purity of the obtained $(R/S-3\text{BrMBA})_3\text{EuCl}_6$ powders (Fig. 1b and Supplementary Fig. 2). The scanning electron microscopy (SEM) images and the energy dispersive spectroscopy (EDS) mappings confirm the uniform distributions of the constituting elements (C, Eu, and Cl) in the $(R-3\text{BrMBA})_3\text{EuCl}_6$ and $(S-3\text{BrMBA})_3\text{EuCl}_6$ microcrystals (Fig. 1c and Supplementary Fig. 3). X-ray photoelectron spectroscopy (XPS) was subsequently employed to investigate the valence state of each element in $(R-3\text{BrMBA})_3\text{EuCl}_6$ and $(S-3\text{BrMBA})_3\text{EuCl}_6$ (Supplementary Figs. 4, 5). The XPS peaks at

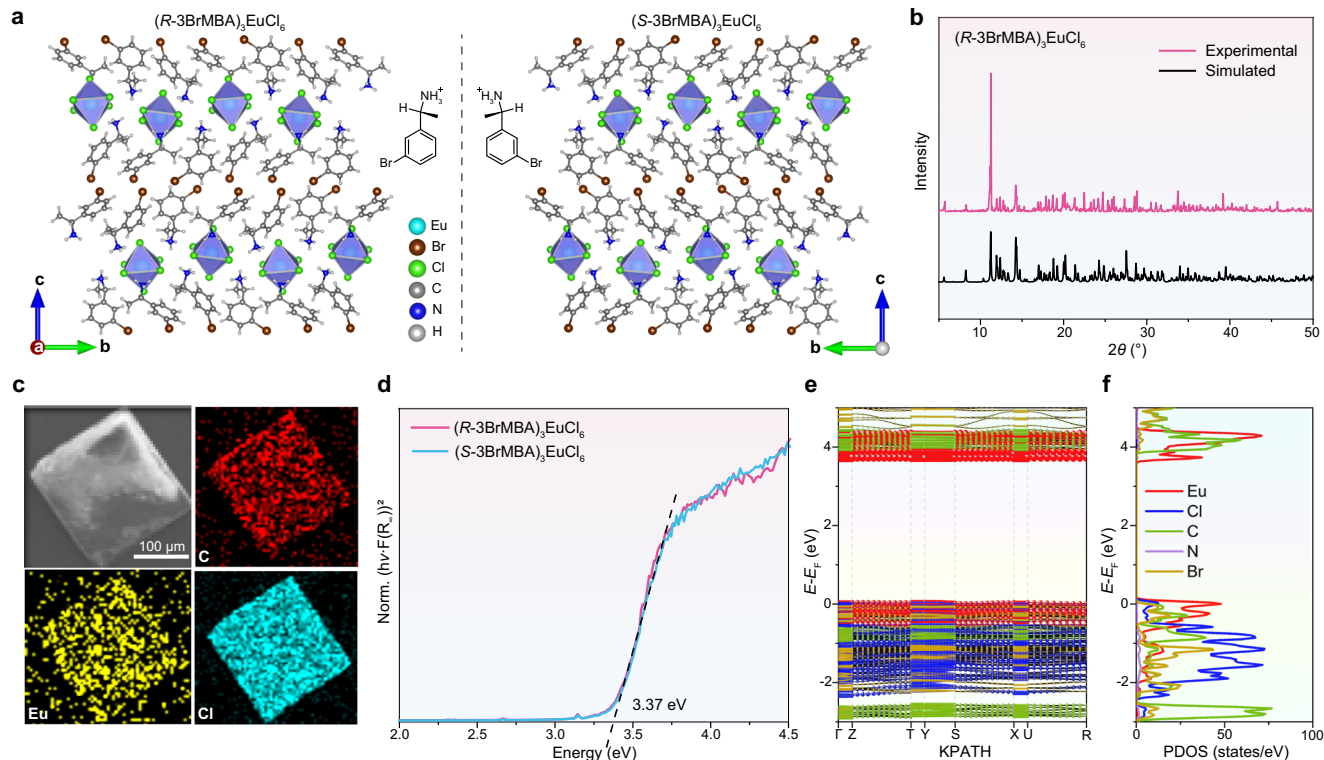


Fig. 1 | Material properties for chiral Eu-based halides. **a** Crystal structures of $(R/S-3\text{BrMBA})_3\text{EuCl}_6$. Eu, Br, Cl, C, N, and H are represented by the light blue, brown, green, dark gray, blue, and light gray spheres, respectively. **b** PXRD patterns of $(R-3\text{BrMBA})_3\text{EuCl}_6$. The pink line is the experimental results, and the black line is the corresponding simulated results from the crystal structure. **c** The SEM image of

$(R-3\text{BrMBA})_3\text{EuCl}_6$ microcrystal and EDS mapping images of C (red), Eu (yellow), and Cl (blue) distributions. **d** Tauc plot to determine the optical bandgaps of $(R-3\text{BrMBA})_3\text{EuCl}_6$ (pink) and $(S-3\text{BrMBA})_3\text{EuCl}_6$ (blue). **e** The calculated electronic band structure of $(R-3\text{BrMBA})_3\text{EuCl}_6$. **f** The calculated PDOS of $(R-3\text{BrMBA})_3\text{EuCl}_6$ (Eu: red line, Cl: blue line, C: green line, N: purple line, Br: yellow line).

approximately 200.1 and 198.4 eV are ascribed to the chloride ions (Cl $2p_{1/2}$ and Cl $2p_{3/2}$) in the inorganic skeleton. The peak at 284.8 eV is assigned to the carbon atoms on the chiral cations (C 1s). The peaks at 401.9 and 399.9 eV stem from the nitrogen atom of the ammonium group (N 1s). Meanwhile, two characteristic peaks of Eu^{3+} at 1136.1 and 1165.9 eV are attributed to the Eu $3d_{5/2}$ and $3d_{3/2}$ spin states, respectively^{53,54}. In addition, the chiral Eu-based halides exhibit good thermal stability (≈ 520 K), as evidenced by the thermogravimetric analysis (TGA) (Supplementary Fig. 6). The ultraviolet-visible (UV-Vis) absorption spectra of $(R\text{-}3\text{BrMBA})_3\text{EuCl}_6$ and $(S\text{-}3\text{BrMBA})_3\text{EuCl}_6$ were also measured and shown in Supplementary Fig. 7, which exhibits almost undistinguishable absorption edges at ca. 379 nm due to their enantiomeric nature. By comparing the absorption spectra of $(R\text{-}3\text{BrMBA})_3\text{EuCl}_6$ and $(S\text{-}3\text{BrMBA})_3\text{EuCl}_6$ with their chiral cations (Supplementary Fig. 8a), it is confirmed that the absorption peak at 270 nm is mainly from the $R/S\text{-}3\text{BrMBA}^+$ cations. Notably, owing to the $4f\text{-}4f$ transitions properties, many characteristic peaks of Eu^{3+} ions were observed in the absorption spectra, which are 395 nm (${}^5\text{L}_6 \leftarrow {}^7\text{F}_0$), 465 nm (${}^5\text{D}_2 \leftarrow {}^7\text{F}_0$), 536 nm (${}^5\text{D}_1 \leftarrow {}^7\text{F}_1$), and 592 nm (${}^5\text{D}_0 \leftarrow {}^7\text{F}_1$)^{51,55}, respectively. According to the Tauc plot, the optical bandgaps of $(R\text{-}3\text{BrMBA})_3\text{EuCl}_6$ and $(S\text{-}3\text{BrMBA})_3\text{EuCl}_6$ are approximately 3.37 eV (Fig. 1d). To further understand the optical properties of $(R/S\text{-}3\text{BrMBA})_3\text{EuCl}_6$, density functional theory (DFT) calculations were performed to explore their optical transitions in detail. The electronic band structure and the corresponding projected density of states (PDOS) for $(R\text{-}3\text{BrMBA})_3\text{EuCl}_6$ were calculated and shown in Fig. 1e, f, and Supplementary Fig. 9. The negligible dispersion of the bands is consistent with the OD structural features. The valence band maximum (VBM) consists of the unpaired $4f$ electrons of Eu atoms and p -orbitals of Cl atoms, while the conduction band minimum (CBM) comprises the $4f$ -orbitals of Eu atoms. The p -orbitals of the C atoms in the chiral organic cations with relatively higher conduction band energies indicate that the chiral cations do not contribute to the optical transitions near the band edges. Nevertheless, they may play a role in the transitions at shorter wavelengths. The results are close in agreement with the aforementioned UV-Vis absorption spectra. Therefore, the $f\text{-}f$ transition dominates the optical properties of $(R/S\text{-}3\text{BrMBA})_3\text{EuCl}_6$ near the band edge.

Chiroptical properties

Europium has been recognized as a magic element in the family of rare-earth metals, and the chiral hybrid europium halides are expected to exhibit excellent chiroptical properties. As shown in Supplementary Fig. 10, the bright red luminescence of $(R/S\text{-}3\text{BrMBA})_3\text{EuCl}_6$ crystals was observed under UV light (365 nm). The photoluminescence excitation (PLE) spectra for $(R/S\text{-}3\text{BrMBA})_3\text{EuCl}_6$ under different emission peaks are shown in Supplementary Figs. 11, 12, which exhibit relatively strong and sharp peaks at 395 and 465 nm in accordance with those of the UV-Vis absorption spectra (Supplementary Fig. 7). The steady-state photoluminescence (PL) spectra of $(R\text{-}3\text{BrMBA})_3\text{EuCl}_6$ and $(S\text{-}3\text{BrMBA})_3\text{EuCl}_6$ have identical features under 465 nm excitation at room temperature (Fig. 2a). The emission peaks at 594, 614, 654, and 704 nm are assigned to the ${}^5\text{D}_0 \rightarrow {}^7\text{F}_1$, ${}^5\text{D}_0 \rightarrow {}^7\text{F}_2$, ${}^5\text{D}_0 \rightarrow {}^7\text{F}_3$, and ${}^5\text{D}_0 \rightarrow {}^7\text{F}_4$ transitions of Eu^{3+} ions, respectively, which have been observed in other Eu(III) compounds as well^{56–58}. Notably, the full width at half maximum (FWHM) at 594 nm is nearly 2 nm for $(R/S\text{-}3\text{BrMBA})_3\text{EuCl}_6$. This is attributed to the $4f$ intra-shell transitions of Eu^{3+} ions shielded by the external $5s$ and $5p$ orbitals, reducing the influence of the surrounding environment on the $4f\text{-}4f$ transitions⁴⁴. The Commission International de l'Éclairage (CIE) coordinates of $(R\text{-}3\text{BrMBA})_3\text{EuCl}_6$ and $(S\text{-}3\text{BrMBA})_3\text{EuCl}_6$ are (0.64, 0.36) and (0.64, 0.36), respectively (Fig. 2b), which are almost close to the standard red emission region (0.67, 0.33) in the National Television Standards Committee (NTSC) standard⁵⁹. Therefore, $(R\text{-}3\text{BrMBA})_3\text{EuCl}_6$ and $(S\text{-}3\text{BrMBA})_3\text{EuCl}_6$ with such high color purity

are promising candidates for the pure-red emitters. The time-resolved photoluminescence (TRPL) spectra as shown in Fig. 2c and Supplementary Fig. 13, the PL lifetime of different emission peaks for $(R\text{-}3\text{BrMBA})_3\text{EuCl}_6$ and $(S\text{-}3\text{BrMBA})_3\text{EuCl}_6$ are mostly around 2 ms at room temperature. The longer lifetime at the ms level arises from the parity-forbidden of the $4f\text{-}4f$ transitions⁴⁵. The PLQYs of $(R\text{-}3\text{BrMBA})_3\text{EuCl}_6$ and $(S\text{-}3\text{BrMBA})_3\text{EuCl}_6$ microcrystals are 56.5% and 59.8% at room temperature, respectively (Fig. 2d and Supplementary Fig. 14). The higher PLQY illustrates the carrier recombination in $(R\text{-}3\text{BrMBA})_3\text{EuCl}_6$ and $(S\text{-}3\text{BrMBA})_3\text{EuCl}_6$ is mainly determined by the radiative recombination, while the non-radiative recombination associated with the defects is negligible⁶⁰.

To further investigate the chiral optical properties of $(R\text{-}3\text{BrMBA})_3\text{EuCl}_6$ and $(S\text{-}3\text{BrMBA})_3\text{EuCl}_6$, the vibrational circular dichroism (VCD) spectra were first measured (Supplementary Fig. 15). The VCD signals of $(R\text{-}3\text{BrMBA})_3\text{EuCl}_6$ and $(S\text{-}3\text{BrMBA})_3\text{EuCl}_6$ are opposite, supporting their enantiomeric structures. Then the circular dichroism (CD) spectra were measured and shown in Fig. 2e. The mirror-symmetric CD signals from 245 to 600 nm further confirm the enantiomeric nature of $(R\text{-}3\text{BrMBA})_3\text{EuCl}_6$ and $(S\text{-}3\text{BrMBA})_3\text{EuCl}_6$. The CD spectra of $R/S\text{-}3\text{BrMBA}$ were also measured and their signals are before 283 nm (Supplementary Fig. 8b). However, when they are incorporated into $(R\text{-}3\text{BrMBA})_3\text{EuCl}_6$ and $(S\text{-}3\text{BrMBA})_3\text{EuCl}_6$, the resulting chiral metal halides exhibit strong CD signals from 283 nm to 600 nm (Fig. 2e). These results indicate that the chirality of the chiral cations is transferred to the inorganic $[\text{EuCl}_6]^{3-}$ framework. To further explore the chiral luminescent properties of $(R\text{-}3\text{BrMBA})_3\text{EuCl}_6$ and $(S\text{-}3\text{BrMBA})_3\text{EuCl}_6$, their CPL spectra were measured and shown in Fig. 2f. Clear mirror-symmetric CPL spectra from 550 to 650 nm were observed, and the CPL peaks are mainly located at ca. 601 nm and 616 nm. They are also consistent with the steady-state PL spectra as discussed above, further indicating that chirality is transferred from chiral cations to the europium halides. The dissymmetry factors (g_{lum}) of CPL for $(R\text{-}3\text{BrMBA})_3\text{EuCl}_6$ and $(S\text{-}3\text{BrMBA})_3\text{EuCl}_6$ are calculated to be -1.84×10^{-2} and 1.18×10^{-2} at 616 nm, respectively⁶¹. To assess the performance of CPL materials, the figure of merit (FOM) is also calculated, which is defined as Eq. (1)^{61,62},

$$\text{FOM} = |g_{\text{lum}}| \times \text{PLQY} \quad (1)$$

The calculated FOM value of $(R\text{-}3\text{BrMBA})_3\text{EuCl}_6$ is 10.40×10^{-3} . Compared with the previously reported chiral metal halides with red CPL emission, $(R\text{-}3\text{BrMBA})_3\text{EuCl}_6$ exhibits the largest FOM values, longer lifetimes, and narrower FWHM (Supplementary Figs. 16–18, and Supplementary Table 2)^{39–43,63}. Therefore, these chiral Eu-based halides are promising candidates for high-performance red CPL emitters.

Magneto-chiroptical properties

The magneto-chiroptical properties of $(R\text{-}3\text{BrMBA})_3\text{EuCl}_6$ and $(S\text{-}3\text{BrMBA})_3\text{EuCl}_6$ were then investigated by temperature- and magnetic-field-dependent degree of photoluminescence polarization (DP). More details about this experiment and the sample preparation method are provided in the Methods section. The DP is evaluated by Eq. (2),

$$\text{DP}(\%) = \frac{I_L - I_R}{I_L + I_R} \times 100\% \quad (2)$$

in which, I_L and I_R are the photoluminescence intensities due to the left- and right-handed circularly polarized photoexcitation, respectively. The temperature-dependent DP from 300 K to 4 K is shown in Fig. 3a, and there are two noticeable phenomena for $(R/S\text{-}3\text{BrMBA})_3\text{EuCl}_6$. DP becomes increasingly larger with decreasing the

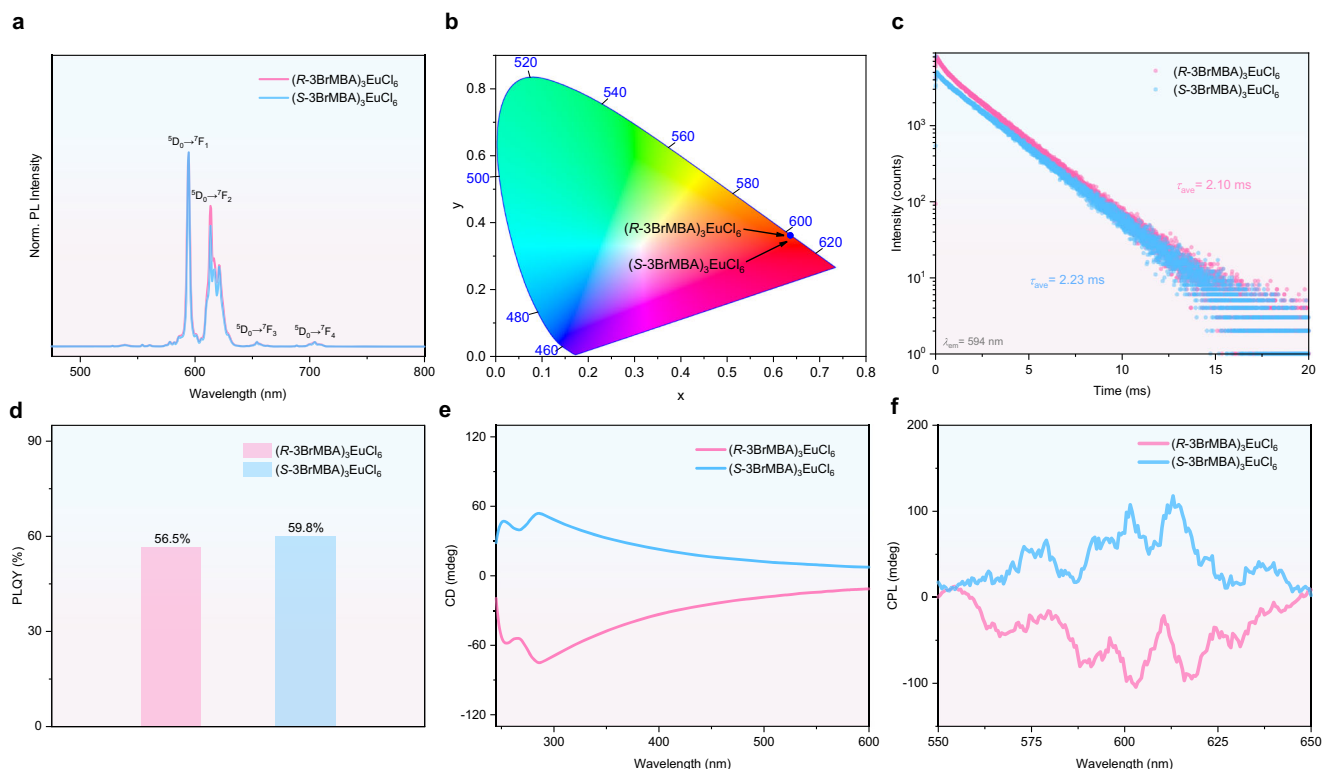


Fig. 2 | Chiroptical properties for chiral Eu-based halides. **a** The normalized steady-state PL spectra of $(R\text{-}3\text{BrMBA})_3\text{EuCl}_6$ (pink) and $(S\text{-}3\text{BrMBA})_3\text{EuCl}_6$ (blue) under 465 nm excitation. **b** The CIE color coordinates diagram of $(R/S\text{-}3\text{BrMBA})_3\text{EuCl}_6$. **c** The TRPL spectra of 594 nm emission for $(R\text{-}3\text{BrMBA})_3\text{EuCl}_6$

(pink) and $(S\text{-}3\text{BrMBA})_3\text{EuCl}_6$ (blue) under 465 nm excitation. τ_{ave} , PL lifetime. **d** The PLQYs of $(R\text{-}3\text{BrMBA})_3\text{EuCl}_6$ (pink) and $(S\text{-}3\text{BrMBA})_3\text{EuCl}_6$ (blue) under 465 nm excitation. **e** The CD spectra of $(R\text{-}3\text{BrMBA})_3\text{EuCl}_6$ (pink) and $(S\text{-}3\text{BrMBA})_3\text{EuCl}_6$ (blue). **f** The CPL spectra of $(R\text{-}3\text{BrMBA})_3\text{EuCl}_6$ (pink) and $(S\text{-}3\text{BrMBA})_3\text{EuCl}_6$ (blue).

temperature. Owing to the implementation of chirality, DP grows in the opposite directions for $(R\text{-}3\text{BrMBA})_3\text{EuCl}_6$ and $(S\text{-}3\text{BrMBA})_3\text{EuCl}_6$. When carriers are moving in the helical structure of $(R\text{-}3\text{BrMBA})_3\text{EuCl}_6$ and $(S\text{-}3\text{BrMBA})_3\text{EuCl}_6$, they may acquire an extra orbital angular momentum^{64,65}. Such momentum can be energetically coupled with the spin of carriers, and lead to the formation of the chirality-induced spin-orbit coupling (CISOC)^{66,67}. The ratio of the photoluminescence intensities under the left- and right-handed circularly polarized photoexcitation can be considered as the ratio for the different number of excitons with opposite angular momenta, such as $\frac{I_L}{I_R} = e^{\frac{\Delta E_{\text{SOC}}}{k_B T}}$. An energy difference (ΔE_{SOC}) between the left- and right-handed spin-polarized excitons due to the CISOC is calculated by Eq. (3),

$$\Delta E_{\text{SOC}} = E_{\text{ex}}(j_z^{\text{ex}} = 1) - E_{\text{ex}}(j_z^{\text{ex}} = -1) = 2\alpha\tau\mathbf{K} = 2\alpha\tau \frac{\sqrt{\epsilon_0}}{c} \omega_0 \quad (3)$$

in which, E_{ex} and j_z^{ex} are the exciton's energy and the projection of the exciton total angular momentum along the z-axis. α represents the CISOC strength, $\tau = \pm 1$ denote the helicities, \mathbf{K} denotes the exciton wavevector, c is the speed of light, ϵ_0 is the electric permittivity, ω_0 is the angular frequency. By including the thermal perturbation effect, it can be further expressed by Eq. (4),

$$\Delta E_{\text{total}} = 2\alpha\tau \frac{\sqrt{\epsilon_0}}{c} \omega_0 + Ak_B T \quad (4)$$

where A is the coefficient due to the thermal perturbation. k_B is the Boltzmann constant. T is the temperature. Since all microcrystals are randomly distributed over a large surface area in the experiment, the orientation average should also be considered. The complete

expression for DP is defined as Eq. (5),

$$\text{DP} = \int_0^{\pi/2} \frac{\cos \theta \sin \theta d\theta}{1 + \cos \theta^2} \frac{e^{\frac{2\alpha\tau\sqrt{\epsilon_0}\omega_0 + Ak_B T}{k_B T} - 1}}{e^{\frac{2\alpha\tau\sqrt{\epsilon_0}\omega_0 + Ak_B T}{k_B T} + 1}} \quad (5)$$

here θ is the angle between the crystal orientation (i.e., c -axis) and the observing direction. The experimental results were fitted by Eq. (5) to extract the α value. After fittings, α was found to be approximately $0.152 \text{ eV}\cdot\text{\AA}$ for $(R/S\text{-}3\text{BrMBA})_3\text{EuCl}_6$. These OD chiral rare-earth halide microcrystals have a competitive α value comparable with that of the prototypical two-dimensional chiral lead halides, for instance $\alpha = 0.400 \text{ eV}\cdot\text{\AA}$ for $(R/S\text{-}MBA)_2\text{PbI}_4$ polycrystalline thin films^{65,68,69}. Besides, we also found that DP can be effectively tuned by applying the external magnetic field (Fig. 3b and Supplementary Fig. 19). Depending on the chirality of $(R/S\text{-}3\text{BrMBA})_3\text{EuCl}_6$, the application of the constant magnetic field such as 900 mT has a positive effect on elevating DP with respect to the zero field for $(R\text{-}3\text{BrMBA})_3\text{EuCl}_6$. Meanwhile, the negative field such as -900 mT leads to the reduction of DP. Such field-dependent DP is vice-versa when the chirality is reversed⁷⁰.

Apart from the temperature- and magnetic-field-dependent DP, we also performed the magneto-photoluminescence (MPL) to further investigate the manipulation of the photoluminescence of $(R/S\text{-}3\text{BrMBA})_3\text{EuCl}_6$ by sweeping the magnetic field. The MPL in percentage is evaluated by Eq. (6),

$$\text{MPL}(\%) = \left(\frac{I(B)}{I(0)} - 1 \right) \times 100\% \quad (6)$$

where, $I(B)$ and $I(0)$ represent photoluminescence intensities measured with and without magnetic fields (B represents the magnetic

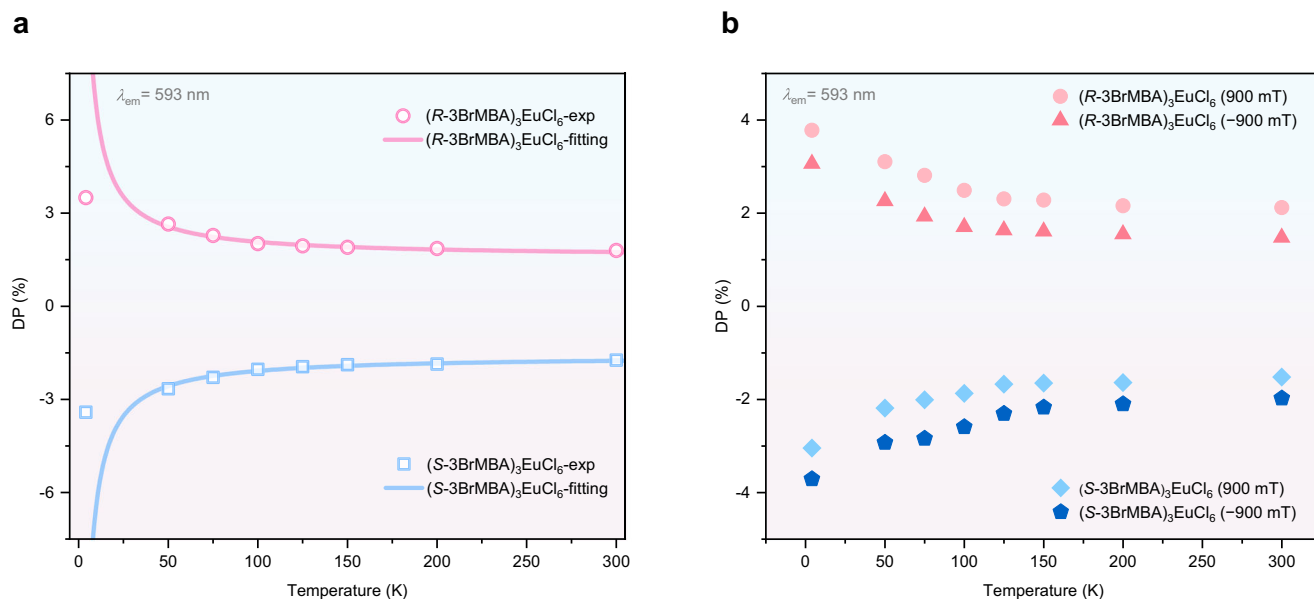


Fig. 3 | Measurements of temperature- and magnetic-field-dependent degree of photoluminescence polarization (DP) for chiral Eu-based halides. a The temperature-dependent DP for the $(R\text{-}3\text{BrMBA})_3\text{EuCl}_6$ (pink circles) and $(S\text{-}3\text{BrMBA})_3\text{EuCl}_6$ (blue squares) measured at 593 nm emission with the absence of applied magnetic fields. The solid lines are the fitting curves for the $(R\text{-}3\text{BrMBA})_3\text{EuCl}_6$ (pink) and $(S\text{-}3\text{BrMBA})_3\text{EuCl}_6$ (blue), respectively. **b** The temperature-dependent DP

for the $(R\text{-}3\text{BrMBA})_3\text{EuCl}_6$ and $(S\text{-}3\text{BrMBA})_3\text{EuCl}_6$ measured at 593 nm emission with applied constant magnetic fields such as ± 900 mT. The pink circles and pink triangles represent the temperature-dependent DP under 900 mT and -900 mT for $(R\text{-}3\text{BrMBA})_3\text{EuCl}_6$, respectively. The blue rhombuses and blue pentagons represent the temperature-dependent DP under 900 mT and -900 mT for $(S\text{-}3\text{BrMBA})_3\text{EuCl}_6$, respectively.

field). The MPL was measured at room temperature and 4 K, respectively, and shown in Fig. 4a, b, and Supplementary Figs. 20, 21. Surprisingly, both $(R\text{-}3\text{BrMBA})_3\text{EuCl}_6$ and $(S\text{-}3\text{BrMBA})_3\text{EuCl}_6$ exhibit an unusual positive MPL effect for the photoluminescence at 591 nm and 612 nm. This MPL effect reaches $\approx 3\%$ for $(R\text{-}3\text{BrMBA})_3\text{EuCl}_6$ and $(S\text{-}3\text{BrMBA})_3\text{EuCl}_6$ at the field strengths of ± 900 mT at room temperature. In fact, this is comparable to the traditional hybrid metal halides, $(\text{PEA})_2\text{PbI}_4$, measured under the same magnetic field at 15 K⁷¹. The reduced temperature (-4 K) has no significant impact on the line shape, sign, and magnitude for this chiral rare-earth metal halide system (Supplementary Fig. 21). Such behavior is indeed very different from the prototypical chiral lead halides such as $(R\text{-}/S\text{-MBA})_2\text{PbI}_4$ ⁶⁸, and achiral metal halides such as $(\text{PEA})_2\text{PbI}_4$ and $(\text{BA})_2\text{PbI}_4$ ⁷¹. In those cases, the effect usually shows a negative sign and it is strongly temperature dependent. Here, we postulate that the positive MPL effect may be ascribed to the spin mixing of the dark and bright exciton states (Fig. 4c). They correspond to the spin singlet ($J=0$, dark states) and triplet ($J=1$, bright states) configurations respectively. Without the magnetic field, these two states are determined by the exchange effect and the Bychkov-Rashba spin-orbit coupling^{72,73}. The applied magnetic field may effectively trigger the Zeeman splitting for the bright states, leading to the mixing of these two states. Consequently, it gives rise to a transfer of excitons from the dark to the bright states. An increase in the bright exciton density may result in the enhancement of the photoluminescence intensity. In this case, the MPL signals were fitted by Eq. (7),

$$\text{MPL}(\%) \propto \left(\frac{1}{4} - \frac{\Delta_{B-D}}{4\sqrt{\Delta_{B-D}^2 + (\Delta g\mu_B B)^2}} \right) \exp\left(-\frac{E-E_F}{k_B T}\right) \quad (7)$$

where Δg is the effective Landé g -factor, μ_B is the Bohr magneton (5.788×10^{-5} eV/T), Δ_{B-D} is the energy splitting of bright states and dark states at 0 mT, E is the energy of bright states at 0 mT, E_F is the Fermi energy level. After fittings, we found Δ_{B-D} is around 11.7 meV, smaller than the reported values for other hybrid metal halides (18–30 meV)⁷⁴.

This indicates that $(R/S\text{-}3\text{BrMBA})_3\text{EuCl}_6$ has relatively smaller exchange effects, and thus the magnetic field could elevate their photoluminescence intensities.

Discussion

In summary, for obtaining high-performance red-CPL emitters, chiral Eu-based halides, $(R\text{-}3\text{BrMBA})_3\text{EuCl}_6$ and $(S\text{-}3\text{BrMBA})_3\text{EuCl}_6$ were designed and constructed by using an anti-solvent assisted crystallization method. Their chiroptical properties were systematically investigated by VCD, CD, and CPL spectra. Combining the $4f\text{-}4f$ transition characteristics of Eu^{3+} ions with chirality, $(R\text{-}3\text{BrMBA})_3\text{EuCl}_6$ and $(S\text{-}3\text{BrMBA})_3\text{EuCl}_6$ exhibit both efficient (PLQY of 59.8%) and narrow red emission (FWHM of ≈ 2 nm), long lifetime (≈ 2 ms), together with high $|g_{\text{lum}}|$ of 1.84×10^{-2} . Compared with the previously reported chiral metal halides with red CPL emission, these chiral Eu-based halides show the highest CPL brightness. Moreover, the degree of photoluminescence polarization in $(R/S\text{-}3\text{BrMBA})_3\text{EuCl}_6$ was further tuned by applying the external magnetic field. Particularly, they exhibit an unusual positive magnetic field effect of $\approx 3\%$ at room temperature, which is comparable to the traditional hybrid metal halide, $(\text{PEA})_2\text{PbI}_4$, measured under the same magnetic field at 15 K. This work offers a strategy to develop the highly-efficient CPL emitter with pure red and sheds light on further exploration of studies on chiral rare-earth halides in spin-optoelectronics.

Methods

Materials

The chemicals including $\text{EuCl}_3 \cdot 6\text{H}_2\text{O}$ (99.99%, MREDA), $(R/S)\text{-}1\text{-}(3\text{-Bromophenyl})\text{ethylamine}$ ($R/S\text{-}3\text{BrMBA}$, 98%, Leyan), hydrochloric acid (HCl, 37%, Aladdin), diethyl ether (99.8%, Tianjin Bohua Chemical Reagent), and methanol (99.9%, SuperDry, J&K Scientific) were used as received without any further purification.

Synthesis of $(R/S\text{-}3\text{BrMBA})_3\text{EuCl}_6$

$\text{EuCl}_3 \cdot 6\text{H}_2\text{O}$ (0.036 g, 0.1 mmol), $R/S\text{-}3\text{BrMBA}$ (0.06 g, 0.3 mmol), and 1 ml HCl were mixed in a flask with 1 mL of methanol. The mixture was

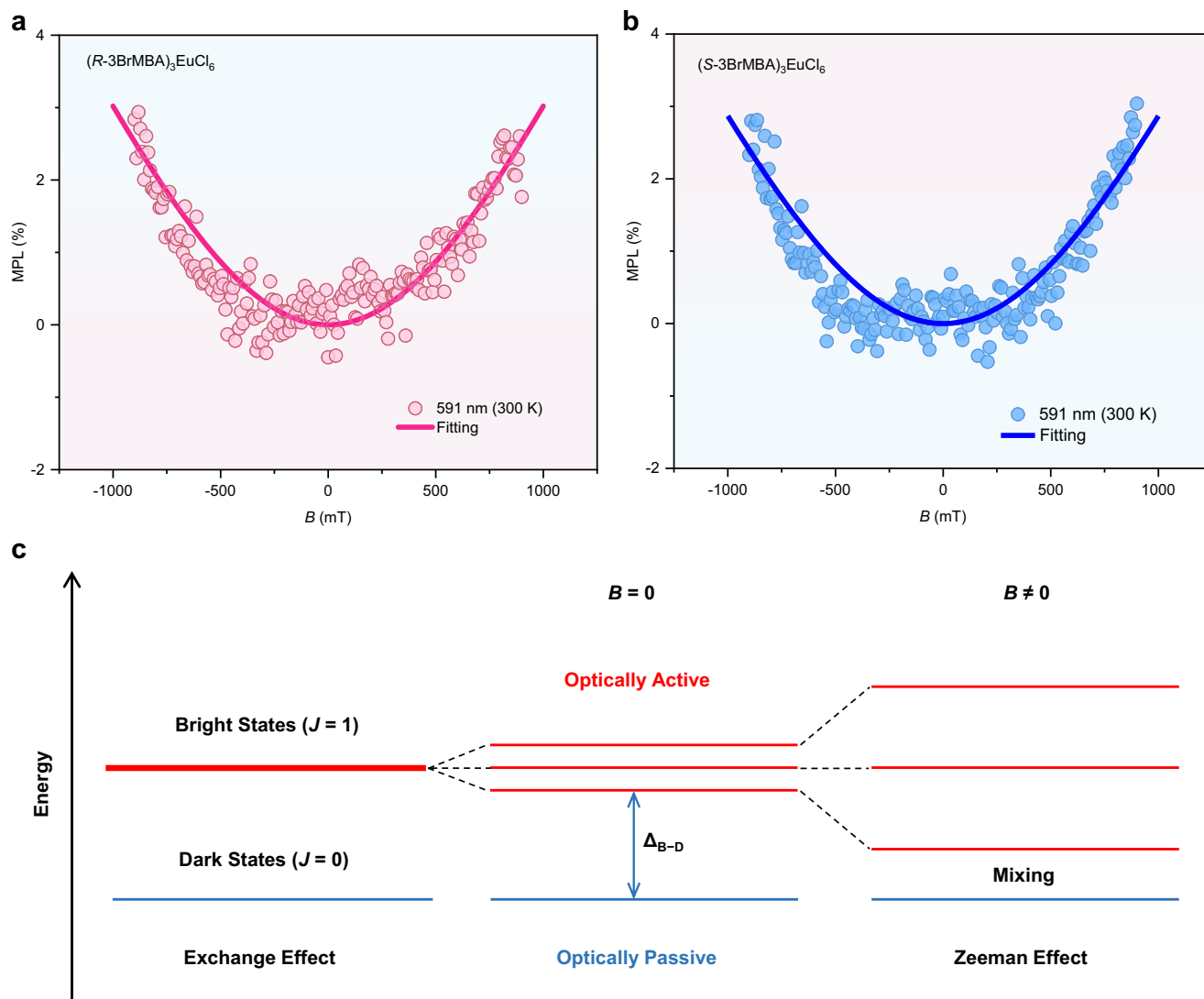


Fig. 4 | Magneto-photoluminescence (MPL) measurements for chiral Eu-based halides. **a, b** The results of MPL for the $(R\text{-}3\text{BrMBA})_3\text{EuCl}_6$ (pink) and $(S\text{-}3\text{BrMBA})_3\text{EuCl}_6$ (blue) measured at 300 K. The solid lines are the fitting

curves. **c** The schematic drawing for the fine structure of exciton states with and without the magnetic field (bright states: red, dark states: dark blue).

heated to 70 °C and stirred for 1 h. Then, the temperature was increased to evaporate the solvent and obtain a solid precursor fully. Afterward, the precursor was dissolved in methanol and crystallized using diethyl ether as the antisolvent to obtain $(R\text{-}3\text{BrMBA})_3\text{EuCl}_6$ and $(S\text{-}3\text{BrMBA})_3\text{EuCl}_6$ crystals.

General characterization

SCXRD data were collected at 100 K on a Rigaku XtaLAB PRO MM007 DW single-crystal X-ray diffractometer ($\text{Mo-K}\alpha$, $\lambda = 0.71073 \text{ \AA}$). The crystal structures were solved using Olex2 software. PXRD patterns were obtained on a Rigaku Smart Lab 3 kW ($\text{Cu K}\alpha$) diffractometer. XPS images were obtained on a Thermo Scientific ESCALAB 250Xi ($\text{Al K}\alpha$) spectrometer. TGA curve was recorded on a METTLER TOLEDO TGA/DSC1 apparatus under N_2 atmosphere with a heating rate of 20 K min^{-1} . SEM images and elemental distributions of the synthesized samples were collected on a JEOL JSM-7800F field-emission scanning electron microscope with an attached energy dispersive spectrometer. VCD spectra were measured on BRUKER PMA50, INVENIO-R vibration circular dichroic-infrared spectrometer by using a mixture of KBr and $(R/S\text{-}3\text{BrMBA})_3\text{EuCl}_6$ pellets. UV-Vis absorption spectra were collected on a Shimadzu UV-2600 UV-Vis spectrometer. An Edinburgh FLS 1000 spectrometer (with a 450 W xenon lamp) was used to measure

the steady-state PL spectra. The TRPL spectra were measured on an Edinburgh FLS1000 fluorescence spectrometer using a microsecond flash lamp at 465 nm. The PLQY was measured by Edinburgh FS5 spectrometer with an integrating sphere, via the absolute method. The samples were excited at 465 nm and the PLQYs were calculated by integrating the PL emission peak. CD spectra were obtained on a JASCO J-1700 CD spectrometer. The mixture of KBr powder and $(R/S\text{-}3\text{BrMBA})_3\text{EuCl}_6$ powder was used and pressed into pellets for CD analysis. The scanning speed is 500 nm min^{-1} , the data pitch is 0.5 nm, and D.I.T is 1 s. CPL spectra were conducted on a JASCO CPL-300 spectrometer. The mixture of KBr powder and $(R/S\text{-}3\text{BrMBA})_3\text{EuCl}_6$ powder was used and pressed into pellets for CPL analysis. The scanning speed is 500 nm min^{-1} , the data pitch is 0.5 nm, and D.I.T is 1 s. The magnetic susceptibility curves of the samples were recorded using a Quantum Design MPMS3 SQUID magnetometer.

Temperature-dependent PL polarization measurement under circularly polarized photoexcitation

The experiment was conducted in a helium-free closed-cycle cryogenic system. Prior to the measurement, some microcrystals either $(R\text{-}3\text{BrMBA})_3\text{EuCl}_6$ or $(S\text{-}3\text{BrMBA})_3\text{EuCl}_6$ were placed on a pre-cleaned glass substrate. They were randomly distributed and encapsulated by a

thin transparent glass. The sample was fixed on a cold finger in the cryogenic system. After sealing the system and pumping it down to a desirable vacuum level, the entire system was inserted in-between a pair of electromagnets with the maximum field strengths of ± 1 T. For every decrement of the temperature from 300 K to 4 K, the microcrystals were photoexcited by a 405 nm continued wave semiconductor laser diode, while the laser beam passed through a polarizer followed by a quarter-wave plate. Fluorescence spectra were captured by a photoluminescence spectrometer with an integrated optical fiber (Model: Horiba Fluorog-3).

MPL measurements

Before the measurement, the sample was mounted on a cold finger in a closed-cycle cryogenic system. The system was pre-pumped to a low vacuum stage. The system could be placed between a pair of electromagnets with a maximum field strength of 1 T. During MPL measurements, the sample is continuously irradiated by a 405 nm laser diode. The PL spectra are collected via an optical fiber and connected to a photoluminescence spectrometer (Model: Horiba Fluorog-3).

Theoretical calculations

The Vienna Ab-initio Simulation Package (VASP) software is used to accomplish the density functional theory (DFT) calculations^{75,76}. The projector augmented wave (PAW) method⁷⁷ with the Perdew-Burke-Ernzerhof functional (PBE)⁷⁸ is selected and the plane-wave cutoff energy is set to 500 eV. Geometric structures are fully relaxed until the energy and total forces are converged to 10^{-5} eV and 10^{-3} eV/Å, respectively. Spin-orbit coupling is considered for accurate electronic structure analysis. VASPKIT code⁷⁹ is used for post-processing analysis.

Reporting summary

Further information on research design is available in the Nature Portfolio Reporting Summary linked to this article.

Data availability

The data that support the findings of this study are available from the corresponding authors upon request. X-ray crystallographic structures have been deposited at the Cambridge Crystallographic Data Center (CCDC), under deposition numbers 2401649 ((*R*-3BrMBA)₃EuCl₆), 2401650 ((*S*-3BrMBA)₃EuCl₆).

References

- Zhang, M. et al. Processable circularly polarized luminescence material enables flexible stereoscopic 3D imaging. *Sci. Adv.* **9**, eadi9944 (2023).
- MacKenzie, L. E. & Pal, R. Circularly polarized lanthanide luminescence for advanced security inks. *Nat. Rev. Chem.* **5**, 109–124 (2020).
- Lin, S. et al. Photo-triggered full-color circularly polarized luminescence based on photonic capsules for multilevel information encryption. *Nat. Commun.* **14**, 3005 (2023).
- Yang, B. et al. Upconversion/downshifting circularly polarized luminescence over 1200 nm in a single nanoparticle for optical anticounterfeiting and information encryption. *Angew. Chem. Int. Ed.* **64**, e202417223 (2024).
- Stachelek, P., MacKenzie, L., Parker, D. & Pal, R. Circularly polarised luminescence laser scanning confocal microscopy to study live cell chiral molecular interactions. *Nat. Commun.* **13**, 553 (2022).
- Zhang, Y. et al. Circularly polarized luminescence in chiral materials. *Matter* **5**, 837–875 (2022).
- Furlan, F. et al. Chiral materials and mechanisms for circularly polarized light-emitting diodes. *Nat. Photonics* **18**, 658–668 (2024).
- Zhang, C., Li, S., Dong, X. Y. & Zang, S. Q. Circularly polarized luminescence of agglomerate emitters. *Aggregate* **2**, e48 (2021).
- Crassous, J. et al. Materials for chiral light control. *Nat. Rev. Mater.* **8**, 365–371 (2023).
- Lu, H., Vardeny, Z. V. & Beard, M. C. Control of light, spin and charge with chiral metal halide semiconductors. *Nat. Rev. Chem.* **6**, 470–485 (2022).
- Yang, Y. et al. Chiral perturbation in D-O-A organic phosphors towards efficient circularly polarized electroluminescence. *Sci. China Mater.* <https://doi.org/10.1007/s40843-024-3042-1> (2024).
- Zhang, D.-W., Li, M. & Chen, C.-F. Axially chiral materials exhibiting blue-emissive ultralong organic phosphorescence and intense circularly polarized luminescence. *Sci. China Mater.* **66**, 4030–4036 (2023).
- Long, G. et al. Chiral-perovskite optoelectronics. *Nat. Rev. Mater.* **5**, 423–439 (2020).
- Chai, C. Y. et al. Single-component white circularly polarized luminescence in chiral 1D double-chain perovskites. *Adv. Opt. Mater.* **11**, 2201996 (2022).
- Guan, J. et al. Free halogen substitution of chiral hybrid metal halides for activating the linear and nonlinear chiroptical properties. *J. Am. Chem. Soc.* **145**, 26833–26842 (2023).
- Guan, Q. et al. Formamidinium engineering the lattice distortion of chiral halide perovskites for efficient blue circularly polarized emission. *Adv. Opt. Mater.* **11**, 2202726 (2023).
- Li, C. et al. Efficient ultraviolet circularly polarized luminescence in zero-dimensional hybrid cerium bromides. *Angew. Chem. Int. Ed.* **63**, e202403727 (2024).
- Song, T. et al. Achieving strong circularly polarized luminescence through cascade cationic insertion in lead-free hybrid metal halides. *Angew. Chem. Int. Ed.* **63**, e202400769 (2024).
- Yang, Z. et al. A universal strategy to enhance circularly polarized luminescence brightness in chiral perovskites. *Laser Photonics Rev.* **18**, 2400040 (2024).
- Li, M. et al. Circularly polarized radioluminescence from chiral perovskite scintillators for improved X-ray imaging. *Angew. Chem. Int. Ed.* **61**, e202208440 (2022).
- Ma, S., Ahn, J. & Moon, J. Chiral perovskites for next-generation photonics: From chirality transfer to chiroptical activity. *Adv. Mater.* **33**, 2005760 (2021).
- Ma, J. et al. Chiral 2D perovskites with a high degree of circularly polarized photoluminescence. *ACS Nano* **13**, 3659–3665 (2019).
- Wei, Q. & Ning, Z. Chiral perovskite spin-optoelectronics and spintronics: Toward judicious design and application. *ACS Mater. Lett.* **3**, 1266–1275 (2021).
- Di Nuzzo, D. et al. Circularly polarized photoluminescence from chiral perovskite thin films at room temperature. *ACS Nano* **14**, 7610–7616 (2020).
- Tang, Y. Y. et al. H/F-substitution-induced homochirality for designing high- T_c molecular perovskite ferroelectrics. *Adv. Mater.* **31**, 1902163 (2019).
- Wang, Q. et al. Spin quantum dot light-emitting diodes enabled by 2D chiral perovskite with spin-dependent carrier transport. *Adv. Mater.* **36**, 2305604 (2023).
- Bai, J. et al. Wafer-scale patterning integration of chiral 3D perovskite single crystals toward high-performance full-stokes polarimeter. *J. Am. Chem. Soc.* **146**, 18771–18780 (2024).
- Ye, C., Jiang, J., Zou, S., Mi, W. & Xiao, Y. Core-shell three-dimensional perovskite nanocrystals with chiral-induced spin selectivity for room-temperature spin light-emitting diodes. *J. Am. Chem. Soc.* **144**, 9707–9714 (2022).
- Kim, K. et al. Chiral-phonon-activated spin Seebeck effect. *Nat. Mater.* **22**, 322–328 (2023).
- Dang, Y., Liu, X., Cao, B. & Tao, X. Chiral halide perovskite crystals for optoelectronic applications. *Matter* **4**, 794–820 (2021).

31. Niu, X. et al. The first chiral cerium halide towards circularly-polarized luminescence in the UV region. *Sci. China Chem.* **67**, 1961–1968 (2024).
32. Cai, W. et al. Chirality induced crystal structural difference in metal halide composites. *Adv. Opt. Mater.* **10**, 2102140 (2022).
33. Zheng, H. et al. Chiral multiferroicity in two-dimensional hybrid organic-inorganic perovskites. *Nat. Commun.* **15**, 5556 (2024).
34. Kim, H. et al. Giant chiral amplification of chiral 2D perovskites via dynamic crystal reconstruction. *Sci. Adv.* **10**, eado5942 (2024).
35. Wei, K., Liang, B., Sun, C., Jiang, Y. & Yuan, M. Metal halide perovskites for red-emission light-emitting diodes. *Small Struct.* **3**, 2200063 (2022).
36. Wu, Y. et al. Lantern-shaped structure induced by racemic ligands in red-light-emitting metal halide with near 100 % quantum yield and multiple-stimulus response. *Angew. Chem. Int. Ed.* **64**, e202416062 (2024).
37. Wang, C. et al. Observation of electron-phonon coupling and linear dichroism in PL spectra of ultra-small CsPbBr₃ nanoparticle solution. *eScience* **3**, 100185 (2023).
38. Guo, Y., Zhang, Y., Ma, J., Liao, R. & Wang, F. Wide-range tunable circularly polarized luminescence in triphenylamine supramolecular polymers via charge-transfer complexation. *Nat. Commun.* **15**, 9303 (2024).
39. Chen, J. et al. Structural origin of enhanced circularly polarized luminescence in hybrid manganese bromides. *Angew. Chem. Int. Ed.* **61**, e202205906 (2022).
40. Gao, J.-X., Zhang, W.-Y., Wu, Z.-G., Zheng, Y.-X. & Fu, D.-W. Enantiomorphic perovskite ferroelectrics with circularly polarized luminescence. *J. Am. Chem. Soc.* **142**, 4756–4761 (2020).
41. Li, J. et al. Circularly polarized luminescence induced by hydrogen-bonding networks in a one-dimensional hybrid manganese(II) chloride. *Angew. Chem. Int. Ed.* **63**, e202405310 (2024).
42. Wang, M. et al. Chiral hybrid manganese(II) halide clusters with circularly polarized luminescence for X-ray imaging. *J. Mater. Chem. C* **11**, 3206–3212 (2023).
43. Xuan, H. L. et al. Amino-acid-induced circular polarized luminescence in one-dimensional manganese(II) halide hybrid. *Chem. Eur. J.* **28**, e202201299 (2022).
44. Chen, P. et al. 2D rare earth material (EuOCl) with ultra-narrow photoluminescence at room temperature. *Small* **17**, 2100137 (2021).
45. Wong, H.-Y., Lo, W.-S., Yim, K.-H. & Law, G.-L. Chirality and chiroptics of lanthanide molecular and supramolecular assemblies. *Chem* **5**, 3058–3095 (2019).
46. Bispo-Jr, A. G., Oliveira, N. A., Diogenis, I. M. S. & Sigoli, F. A. Perspectives and challenges in circularly polarized luminescence of lanthanide(III) complexes: From solution-based systems to solid-state applications. *Coord. Chem. Rev.* **523**, 216279 (2025).
47. Zhong, Y., Wu, Z., Zhang, Y., Dong, B. & Bai, X. Circularly polarized luminescence of lanthanide complexes: From isolated individuals, discrete oligomers, to hierarchical assemblies. *InfoMat* **5**, e12392 (2023).
48. Zeng, Z. et al. Rare-earth-containing perovskite nanomaterials: design, synthesis, properties and applications. *Chem. Soc. Rev.* **49**, 1109–1143 (2020).
49. Yang, L., Luo, J., Gao, L., Song, B. & Tang, J. Inorganic lanthanide compounds with f-d transition: From materials to electroluminescence devices. *J. Phys. Chem. Lett.* **13**, 4365–4373 (2022).
50. Zheng, B. et al. Rare-earth doping in nanostructured inorganic materials. *Chem. Rev.* **122**, 5519–5603 (2022).
51. Binnemans, K. Interpretation of europium(III) spectra. *Coord. Chem. Rev.* **295**, 1–45 (2015).
52. Lu, H. et al. Chiral ruthenium halide semiconductor with strong antiferromagnetic coupling. *Adv. Funct. Mater.* **34**, 2308862 (2023).
53. Zhang, P. et al. Sorption of Eu(III) on MXene-derived titanate structures: The effect of nano-confined space. *Chem. Eng. J.* **370**, 1200–1209 (2019).
54. Rao, Z., Zhao, X. & Gong, X. Modeling of a single-band-ratiometric sensor based on lattice positive thermal expansion in Eu³⁺-activated halide perovskite Cs₂NaEuCl₆. *Small* **20**, 2406348 (2024).
55. Wang, N. et al. Molecular engineering regulation achieving out-of-plane polarization in rare-earth hybrid double perovskites for ferroelectrics and circularly polarized luminescence. *Angew. Chem. Int. Ed.* **63**, e202409796 (2024).
56. Zinna, F. et al. Design of lanthanide-based OLEDs with remarkable circularly polarized electroluminescence. *Adv. Funct. Mater.* **27**, 1603719 (2016).
57. Zinna, F., Giovanella, U. & Bari, L. D. Highly circularly polarized electroluminescence from a chiral europium complex. *Adv. Mater.* **27**, 1791–1795 (2015).
58. Wang, C.-F. et al. Achieving circularly polarized luminescence and large piezoelectric response in hybrid rare-earth double perovskite by a chirality induction strategy. *Mater. Horiz.* **9**, 2450–2459 (2022).
59. Meng, G. et al. B-N covalent bond embedded double hetero-[n] helicenes for pure red narrowband circularly polarized electroluminescence with high efficiency and stability. *Adv. Mater.* **36**, 2307420 (2023).
60. Bai, T. et al. From dopant to host: Solution synthesis and light-emitting applications of organic-inorganic lanthanide-based metal halides. *Small Struct.* **5**, 2400096 (2024).
61. Yao, L. et al. Circularly polarized luminescence from chiral tetranuclear copper(I) iodide clusters. *J. Phys. Chem. Lett.* **11**, 1255–1260 (2020).
62. Yuan, Y.-X., Zhang, J.-N., Wang, J.-R., Li, K. & Zang, S.-Q. Chiral silver cluster-based light-harvesting systems: Enantioselective chirality transfer and amplified circularly polarized luminescence. *Chem* **10**, 1766–1782 (2024).
63. Yang, C.-H., Xiao, S.-B., Xiao, H., Xu, L.-J. & Chen, Z.-N. Efficient red-emissive circularly polarized electroluminescence enabled by quasi-2D perovskite with chiral spacer cation. *ACS Nano* **17**, 7830–7836 (2023).
64. Yang, S.-H., Naaman, R., Paltiel, Y. & Parkin, S. S. P. Chiral spintronics. *Nat. Rev. Phys.* **3**, 328–343 (2021).
65. Yu, Z.-G. Chirality-induced spin-orbit coupling, spin transport, and natural optical activity in hybrid organic-inorganic perovskites. *J. Phys. Chem. Lett.* **11**, 8638–8646 (2020).
66. Tang, J. et al. Chiral ionic liquids enable high-performance room temperature single junction spin-light emitting diodes. *Laser Photonics Rev.* **19**, 2401008 (2025).
67. Li, B. et al. Chiral quasi-2D perovskites based single junction spin-light-emitting diodes. *Adv. Funct. Mater.* **35**, 2415433 (2024).
68. Pan, R., Wang, K. & Yu, Z.-G. Magnetic-field manipulation of circularly polarized photoluminescence in chiral perovskites. *Mater. Horiz.* **9**, 740–747 (2022).
69. Pan, R., Tao, S., Wang, K. & Yu, Z.-G. Experimental and theoretical studies of magnetic circular dichroism for chiral lead halide perovskites. *Chem. Mater.* **35**, 1667–1673 (2023).
70. Long, G. et al. Spin control in reduced-dimensional chiral perovskites. *Nat. Photonics* **12**, 528–533 (2018).
71. Bailey, C. G. et al. Influence of organic spacer cation on dark excitons in 2D perovskites. *Adv. Funct. Mater.* **34**, 2308095 (2023).
72. Yu, Z.-G. The Rashba effect and indirect electron-hole recombination in hybrid organic-inorganic perovskites. *Phys. Chem. Chem. Phys.* **19**, 14907–14912 (2017).
73. Yu, Z.-G. Effective-mass model and magneto-optical properties in hybrid perovskites. *Sci. Rep.* **6**, 28576 (2016).
74. Dyksik, M. et al. Brightening of dark excitons in 2D perovskites. *Sci. Adv.* **7**, eabk0904 (2021).

75. Kresse, G. & Furthmüller, J. Efficiency of ab-initio total energy calculations for metals and semiconductors using a plane-wave basis set. *Comp. Mater. Sci.* **6**, 15–50 (1996).
76. Kresse, G. & Furthmüller, J. Efficient iterative schemes for ab initio total-energy calculations using a plane-wave basis set. *Phys. Rev. B* **54**, 11169–11186 (1996).
77. Blöchl, P. E. Projector augmented-wave method. *Phys. Rev. B* **50**, 17953–17979 (1994).
78. Perdew, J. P., Burke, K. & Ernzerhof, M. Generalized gradient approximation made simple. *Phys. Rev. Lett.* **77**, 3865–3868 (1996).
79. Wang, V., Xu, N., Liu, J.-C., Tang, G. & Geng, W.-T. VASPKIT: A user-friendly interface facilitating high-throughput computing and analysis using VASP code. *Comput. Phys. Commun.* **267**, 108033 (2021).

Acknowledgements

The authors gratefully acknowledge the financial support from the National Key R&D Program of China (2024YFA1209603) (K.W.), the NSFC (Grant Number: 52473305, 92256202, 22371131, 12261131500, 62174079) of China (G.L., Y.D., K.W.), the National Science Foundation for Distinguished Young Scholars of China (22425503), the Outstanding Youth Project of Tianjin Natural Science Foundation (20JCJQC00130), the Key Laboratory of Rare Earths, Chinese Academy of Sciences, the Fundamental Research Funds for the Central Universities, Nankai University (Grant Number: 023-63233038) (G.L.), the Natural Science Foundation of Guangdong Province (2022A1515011246) (G.L.), the 111 Project (B18030) (G.L.), the Fundamental Research Funds for the Central Universities, Key Project (2023JBZY002) (K.W.), the Tangshan Science and Technology Bureau (23130226E) (K.W.), and the Natural Science Foundation of Hebei Province (F2024105019) (K.W.). All the theoretical calculations were performed on National Supercomputer Center in Guangzhou.

Author contributions

G.L., K.W., and Y.D. conceived and directed the project. X.N. conducted the synthesis and characterization. Y.L. carried out the measurements under the magnetic field. H.L. contributed theory calculations. T.S. helped with the SEM measurements, X.N., Y.L., K.W., and G.L. wrote the manuscript, Z.W., Y.Z., H.W., S.G., B.S., Y.D., H.L.Z., and Y.C. contributed to the discussion and revising of the manuscript.

Competing interests

The authors declare no competing interests.

Additional information

Supplementary information The online version contains supplementary material available at <https://doi.org/10.1038/s41467-025-57620-0>.

Correspondence and requests for materials should be addressed to Kai Wang, Yaping Du or Guankui Long.

Peer review information *Nature Communications* thanks the anonymous reviewer(s) for their contribution to the peer review of this work. A peer review file is available.

Reprints and permissions information is available at <http://www.nature.com/reprints>

Publisher's note Springer Nature remains neutral with regard to jurisdictional claims in published maps and institutional affiliations.

Open Access This article is licensed under a Creative Commons Attribution-NonCommercial-NoDerivatives 4.0 International License, which permits any non-commercial use, sharing, distribution and reproduction in any medium or format, as long as you give appropriate credit to the original author(s) and the source, provide a link to the Creative Commons licence, and indicate if you modified the licensed material. You do not have permission under this licence to share adapted material derived from this article or parts of it. The images or other third party material in this article are included in the article's Creative Commons licence, unless indicated otherwise in a credit line to the material. If material is not included in the article's Creative Commons licence and your intended use is not permitted by statutory regulation or exceeds the permitted use, you will need to obtain permission directly from the copyright holder. To view a copy of this licence, visit <http://creativecommons.org/licenses/by-nc-nd/4.0/>.

© The Author(s) 2025

¹Tianjin Key Lab for Rare Earth Materials and Applications, Center for Rare Earth and Inorganic Functional Materials, Frontiers Science Center for New Organic Matter, Haihe Laboratory of Sustainable Chemical Transformations, School of Materials Science and Engineering, National Institute for Advanced Materials, Nankai University, Tianjin, China. ²Key Laboratory of Luminescence and Optical Information, Ministry of Education, School of Physical Science and Engineering, Beijing Jiaotong University, Beijing, China. ³Institute of Optoelectronics Technology, Beijing Jiaotong University, Beijing, China. ⁴State Key Laboratory of Applied Organic Chemistry (SKLAOC), College of Chemistry and Chemical Engineering, Lanzhou University, Lanzhou, China. ⁵State Key Laboratory and Institute of Elemento-Organic Chemistry, Frontiers Science Center for New Organic Matter, Nankai University, Tianjin, China. ⁶The Centre of Nanoscale Science and Technology and Key Laboratory of Functional Polymer Materials, College of Chemistry, Nankai University, Tianjin, China. ⁷These authors contributed equally: Xinyi Niu, Yang Li. ✉ e-mail: kaiwang@bjtu.edu.cn; ypdu@nankai.edu.cn; longgk09@nankai.edu.cn